

Communication

Polymers and Plastrons in Parallel Yield Enhanced Turbulent Drag Reduction

Anoop Rajappan  and Gareth H. McKinley * 

Hatsopoulos Microfluids Laboratory, Department of Mechanical Engineering, Massachusetts Institute of Technology, Cambridge, MA 02139, USA; anoopr@mit.edu

* Correspondence: gareth@mit.edu

Received: 13 October 2020; Accepted: 29 October 2020; Published: 1 November 2020



Abstract: Despite polymer additives and superhydrophobic walls being well known as stand-alone methods for frictional drag reduction in turbulent flows, the possibility of employing them simultaneously in an additive fashion has remained essentially unexplored. Through experimental friction measurements in turbulent Taylor–Couette flow, we show that the two techniques may indeed be combined favorably to generate enhanced levels of frictional drag reduction in wall-bounded turbulence. We further propose an additive expression in Prandtl–von Kármán variables that enables us to quantitatively estimate the magnitude of this cooperative drag reduction effect for small concentrations of dissolved polymer.

Keywords: drag reduction; polymers; superhydrophobic surfaces; Taylor–Couette turbulence

1. Introduction

Wall-bounded turbulent flows play a ubiquitous role in modern engineering and industry, in applications ranging from the internal flow of liquids in pipelines, to the external boundary layer flow around the hulls of ships and submarines [1,2]. The mitigation of frictional losses in turbulent flows is thus of considerable practical interest, with the potential to confer significant economic and environmental benefits. The systematic modification of turbulence dynamics through the introduction of either dissolved polymer chains [3–7] or boundary slip [8–10], leading to drag reduction, remains an active area of research and has witnessed resurgent interest in recent years [11–13]. The addition of soluble, high molar mass polymers has long been known to be an effective strategy for reducing frictional drag in turbulent flows [14–16]. Even at dilute concentrations as low as 10 ppm, dissolved long-chain polymers can interact with and alter near-wall coherent flow structures, yielding concomitant reductions in the frictional wall shear stress of 20–40% [12–16]. A wide range of synthetic as well as naturally occurring high polymers have been successfully employed as drag reducing agents in a variety of turbulent flow configurations [17,18].

In recent years, superhydrophobic texturing of submerged solid surfaces has also emerged as a viable method of drag reduction in wall-bounded aqueous flows [19–22]. Superhydrophobic walls incorporate hydrophobic micro-textural features capable of thermodynamically stabilizing a thin layer of air—called the *plastron*—that remains pinned to the texture asperities in the Cassie–Baxter state, even when fully submerged underwater [19,20]. This intervening gas layer, in turn, shields the liquid from direct contact with the underlying solid substrate over large areal fractions of the flow boundary. Even as the usual no-slip condition continues to apply in regions of solid–liquid contact, the liquid–air interface atop the plastron layer serves as a nearly shear-free boundary over which the flow slips with minimal friction. The effect of this composite boundary on the outer flow is often modeled as an equivalent uniform slip velocity V_s at the wall, given by the Navier slip condition $V_s = b \tau_w / \eta$; here η is the dynamic viscosity of the liquid, τ_w the shear stress at the wall, and b represents an average

“effective” slip length characterizing the superhydrophobic texture [20]. Despite early successes in laminar drag reduction as far back as 1996 [23], progress towards the use of superhydrophobic surfaces in turbulent flows has been slow, due in part to challenges in fabricating robust textures capable of sustaining an intact plastron layer even under the intense pressure fluctuations typically encountered in turbulence [22,24]. Several robust surfaces have, nevertheless, been developed in recent years, and turbulent drag reductions of up to 50% on periodically micropatterned surfaces, and up to 30% on scalable, randomly textured surfaces, have been reported in the open literature [22,25,26].

Consequently, we now have available two independent physical mechanisms for realizing practicable levels of drag reduction in turbulent flows: (i) dissolved polymer chains, which alter near-wall flow dynamics and disrupt turbulence production in the boundary layer, and (ii) plastron-supporting superhydrophobic surfaces, which enable diminished wetted contact of the fluid with the solid boundary, effectively inducing a slip velocity at the wall. Insofar as these physical mechanisms operate via fundamentally distinct pathways, a natural question arises as to whether the two approaches may be employed concurrently to yield enhanced reductions in frictional drag. Rather surprisingly, this possibility has remained largely unexplored in the extant literature. The only prior instance of polymers being used in conjunction with superhydrophobic textures for drag reduction seems to be an early experimental study by Watanabe and Udagawa [23], who measured the frictional pressure drop of aqueous polyethylene oxide (PEO) solutions in a circular pipe treated with a water-repellent coating. Although they separately observed wall slip in the laminar regime and polymer drag reduction in the turbulent regime, no combined effect arising from the two mechanisms operating in concert was reported, presumably due to the loss of entrapped gas from their superhydrophobic texture leading to plastron collapse in the turbulent regime. Recently, Davis and Park [27] presented direct numerical simulations of viscoelastic turbulent channel flow in the presence of wall slip; their preliminary results, however, indicated a slip-induced increase in the apparent drag.

In this paper, we answer the above question in the affirmative, and show that polymers and superhydrophobic textures can indeed be combined additively to yield enhanced drag reduction in turbulent flows. To this end, we perform experimental measurements of frictional drag in turbulent Taylor–Couette (TC) flow, using a superhydrophobic rotor comprising a periodic array of streamwise grooves, in parallel with a drag-reducing polymer (polyacrylamide) added to the working fluid (water) in the cell gap. Finally, we derive an additive expression to quantitatively estimate this combined drag reduction effect, which yields accurate predictions for low concentrations of the dissolved polymer.

2. Materials and Methods

2.1. Experimental Skin Friction Measurements

Experimental measurements of frictional drag in turbulent flow were performed using a bespoke TC apparatus with an improved design based on the wide-gap TC geometry introduced by Srinivasan et al. [28]. Since the construction and operational features of the TC apparatus are fully detailed elsewhere [26,29], we include here only a brief description of its key components: the rotating inner cylinder (rotor) of radius R_i and length L is housed concentrically inside the stationary outer cylinder (stator) of radius R_o , creating an annular gap of width $d = R_o - R_i$ to which the flow is confined; the radius ratio of our TC geometry is $R_i/R_o = 0.75$, and the gap aspect ratio is $L/d = 6.0$. The rotor is coupled to a commercial rotational rheometer (AR-G2, TA Instruments), enabling precise measurement of the steady-state frictional torque \mathcal{T} exerted on the rotor as a function of its angular speed Ω .

As per the usual convention for TC flows, we define the Reynolds number $Re = \rho V d / \eta$ based on the gap width d , the azimuthal speed $V = R_i \Omega$ of the rotor wall, and the density ρ and viscosity η of the working fluid. As the angular speed Ω of the rotor is increased, the flow inside the TC gap progresses through a sequence of intermediate vortical states, and eventually transitions to featureless (Newtonian) turbulence when a critical Reynolds number, Re_c , is reached. For our TC geometry,

this latter transition to turbulent wall-driven shear flow occurs near $Re_c = 11,000$, as determined from the power-law scaling of the baseline torque \mathcal{T}_N with the Reynolds number Re when measured on a smooth no-slip rotor in deionized water (additional details are provided in the Supplementary Materials). Flow measurements employing polymers or superhydrophobic surfaces were subsequently performed at $Re \geq 15,000$, well into the turbulent flow regime; a typical experiment consists of varying the angular speed Ω of the rotor in discrete steps, and recording the mean steady-state frictional torque \mathcal{T} . The average shear stress $\tau_w = \mathcal{T}/2\pi R_i^2 L$ at the rotor wall, and the friction velocity $u_\tau = \sqrt{\tau_w/\rho}$ in the near-wall layer, were then obtained from the experimental data. Finally, we computed the shear Reynolds number based on the gap width as $Re_\tau = \rho u_\tau d/\eta$, with the reference viscosity η set equal to either the viscosity of water η_w , or—in tests involving drag-reducing polymers—the zero shear viscosity η_0 of the dilute solution employed as the working fluid; the latter was determined independently using an Ubbelöhde type glass capillary viscometer. Tests were conducted at room temperature, $(23.0 \pm 0.5)^\circ\text{C}$, and multiple replicates were obtained for each flow curve and averaged.

2.2. Fabrication of the Superhydrophobic Grooved Surface

To fabricate the superhydrophobic grooved surface, rectangular microgrooves were machined into the surface of the aluminum 6061-T6 rotor using a CNC lathe; the grooves were aligned in the circumferential direction, and spaced evenly along the rotor axis. The rotor was subsequently dip-coated in a $\simeq 0.1\%$ solution of a fluoropolymer resin (Teflon AF 2400, Chemours), and then cured on a laboratory hot plate at 240°C . The dip-coating and baking steps were repeated at least five times to produce a mechanically durable coating firmly attached to the underlying grooves. Scanning electron microscope (SEM) images of the grooves were recorded at multiple spots on the rotor surface, and analyzed to determine the spatial periodicity (and thereby the wetted solid fraction) for the groove pattern. Water droplets were observed to be highly mobile over the final groove pattern, with roll-off occurring at very small ($<5^\circ$) angles.

2.3. Preparation of Polyacrylamide Solutions

Polyacrylamide (PAM) was procured in powder form from Sigma-Aldrich, Inc., and used without further purification. A 0.4% stock solution was first prepared by dispersing the powder in deionized water, and allowing it to hydrate and dissolve gradually on a laboratory bench-roller over several days to ensure homogeneous laminar mixing. Solutions of different concentrations in the range $10\text{ ppm} \leq c \leq 200\text{ ppm}$, for use in flow tests, were then prepared by diluting this stock solution with an appropriate volume of deionized water. Our dilute solutions have elasticity numbers of the order of $El = \lambda\eta/\rho d^2 \simeq 4 \times 10^{-6}$, where λ is the (Zimm) relaxation time of the polymer; the Weissenberg number $Wi = El \cdot Re$ in our experiments therefore ranges from $Wi \simeq 6 \times 10^{-2}$ at $Re = 15,000$, to $Wi \simeq 0.2$ at $Re = 52,000$.

3. Results

Below, we discuss and compare turbulent drag measurements in Newtonian and viscoelastic TC flows, with and without a superhydrophobic texture present at the inner wall. For clarity, results are organized into four sections based on the working fluid inside the gap (i.e., water or polymer solution), and the flow boundary condition (no-slip or superhydrophobic) at the rotor surface.

3.1. Water + No-Slip Rotor

In fully turbulent TC flow of a Newtonian fluid, Panton [30] used matched asymptotic expansions for the azimuthal angular momentum to derive a logarithmic friction law of the form

$$V_N^+ = M \ln Re_\tau + N, \quad (1)$$

where $V^+ = V/u_\tau$ is the rotor wall speed in inner units, the subscript ‘ N ’ denotes Newtonian flow, and M and N are constants determined by the radius ratio of the TC geometry (for an alternative derivation of the logarithmic friction law, see Refs. [31,32]). In Figure 1a, data from flow measurements are presented in Prandtl–von Kármán coordinates, as a plot of V^+ against Re_τ on semi-logarithmic axes. The friction data for a smooth no-slip rotor in deionized water (empty black circles in Figure 1a) in the fully turbulent regime show good conformance to the functional form predicted by Equation (1), and we used a linear least squares regression of the baseline data to obtain the constants $M = 4.76$ and $N = -10.0$ for our bespoke TC geometry.

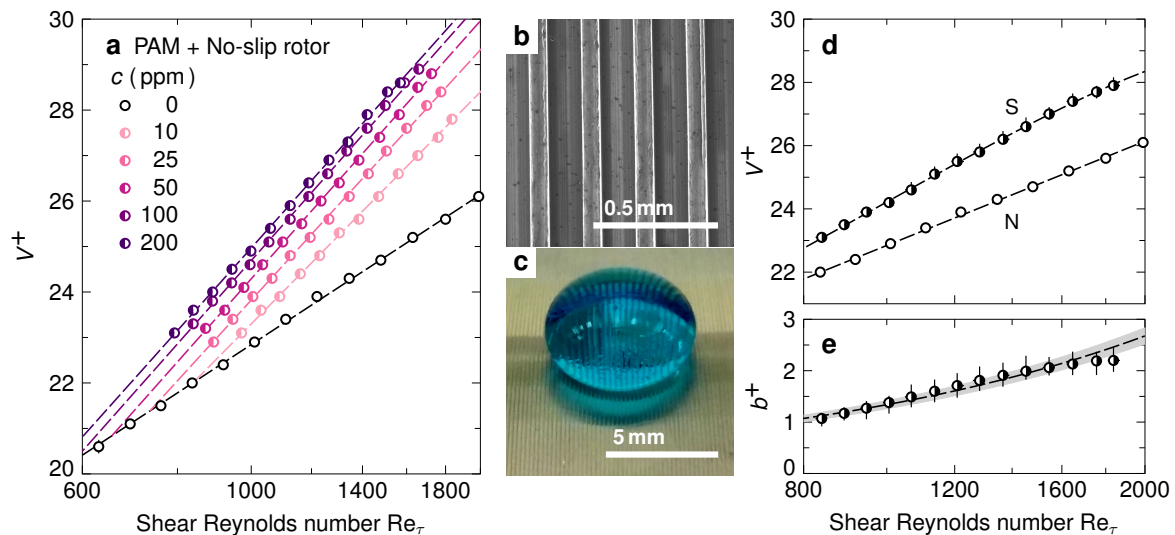


Figure 1. (a) Polymeric drag reduction curves for the no-slip rotor in aqueous polyacrylamide (PAM) solutions (concentration labeled in ppm). The hollow circles denote baseline friction in pure water. (b) SEM image of the grooved rotor surface. (c) Water drop, dyed blue, placed on the grooved rotor. The plastron within the groove troughs appears enlarged due to refraction through the drop. (d) Superhydrophobic drag reduction curve (S) for the grooved rotor in deionized water; the baseline no-slip data (N) from (a) is also included for comparison. (e) The dimensionless effective slip length b^+ measured on the grooved rotor. The dashed curve and the gray band denote the expected variation of b^+ for a constant dimensional slip length of $b = (17 \pm 1) \mu\text{m}$. Error bars represent the full range of observations over 10 replicates.

3.2. Polymer Solution + No-Slip Rotor

As a model drag-reducing polymer system, we employed dilute solutions of aqueous polyacrylamide or PAM, composed of flexible, non-ionic, linear chains of large ($\geq 10^6 \text{ g mol}^{-1}$) molar mass. The intrinsic viscosity of this PAM solution, which we determined experimentally using capillary viscometry and Huggins–Kraemer extrapolation, was $[\eta] = 7.26 \text{ dL g}^{-1}$ at 20°C ; using the Mark–Houwink–Sakurada expressions for PAM available in the literature [33], we inferred a viscosity-averaged molar mass of approximately $M_v \approx 2.54 \times 10^6 \text{ g mol}^{-1}$ for our polymer sample (see Supplementary Materials for details). The critical chain overlap concentration for aqueous PAM may be evaluated [34] as $c^* = 0.77/[\eta] = 1.06 \text{ g L}^{-1}$; the solutions used in our flow tests were considerably more dilute, with concentrations c in the range of 10–200 ppm, corresponding to normalized concentrations of $0.009 \leq c/c^* \leq 0.2$.

Figure 1a shows turbulent friction measurements on a smooth rotor in dilute PAM solutions of different concentrations. As in the Newtonian case, the data are again well described by straight line fits on the Prandtl–von Kármán plot of the form

$$V_P^+ = M_P \ln Re_\tau + N_P, \tag{2}$$

where the subscript ‘*P*’ denotes polymeric turbulence, and the constants M_P and N_P obtained from the fit now depend also on the polymer used and its concentration c in solution. The drag-reducing effect of the dissolved polymer appears as a higher slope and an upward divergence of the polymeric friction curves from the Newtonian baseline in the turbulent regime. This becomes more evident if we consider the non-dimensional skin friction coefficient $C_f = 2\tau_w/\rho V^2$, which may equivalently be expressed as $C_f = 2/(V^+)^2$; a larger V^+ therefore implies a smaller value of C_f , and by extension, a reduced wall shear stress τ_w , at the same imposed speed V at the rotor wall. As expected, the extent of drag reduction increases with increasing Reynolds number, and at higher concentrations of the dissolved polymer; the PAM solution with the highest polymer concentration ($c = 200$ ppm, $c/c^* = 0.2$) approaches the maximum drag reduction limit for our TC geometry at large Reynolds numbers, as discussed in the Supplementary Materials.

3.3. Water + Superhydrophobic Rotor

To obtain a robust plastron-bearing texture with repeatable wall slip characteristics, the surface of the aluminum rotor was machined to produce a regular array of parallel rectangular microgrooves aligned in the circumferential (streamwise) direction, similar to the grooved profile used by Van Buren and Smits [35]. The surface was then coated with a water-repellent fluoropolymer resin, yielding a superhydrophobic grooved texture (Figure 1b) with an average spatial periodicity of $l = 204$ μm and a gas fraction of $\phi = 0.66$ (see Section 2.2 under ‘Materials and Methods’ for details). Figure 1c shows a sessile water drop atop the superhydrophobic rotor surface, and the individual plastrons bridging the groove crests are clearly discernible.

Figure 1d shows experimental drag measurements on the grooved superhydrophobic rotor in deionized, air-saturated water; unlike the polymeric case, the friction curve does not approach the Newtonian, no-slip baseline at Reynolds numbers approaching Re_c , reflecting the fact that superhydrophobic drag reduction is effective in both the turbulent and laminar flow regimes. The skin friction law for fully turbulent TC flow of a Newtonian fluid with a slip boundary at the inner wall may be expressed as [28]

$$V_S^+ = M \ln Re_\tau + N + b^+, \quad (3)$$

where the subscript ‘*S*’ denotes a superhydrophobic wall, $b^+ = b Re_\tau/d$ is the effective slip length expressed in wall units, and the constants M and N are identical to those in Equation (1). In Figure 1e, the non-dimensional slip length b^+ computed from the friction curve using Equation (3) is shown for shear Reynolds numbers $Re_\tau \geq 800$; the data is seen to be well described by a constant slip length of $b = 17$ μm , over the finite range of Reynolds numbers investigated in our study. Except for localized plastron depletion observed in a few grooves and isolated spots at large rotor speeds (leading to the slight decrease in measured slip length at large Re_τ seen in Figure 1e), the maintenance of the plastron layer on the grooved surface was visually confirmed at the end of each experiment.

In the limit of viscosity-dominated creeping flows, the slip length due to an alternating pattern of no-slip and shear-free stripes is given by $b_{\parallel} = (l/\pi) \ln [\sec(\pi\phi/2)]$ parallel to the stripe direction, and $b_{\perp} = b_{\parallel}/2$ perpendicular to it [36]. The situation is more complex in turbulent flows, wherein spanwise slip serves to strengthen near-wall vortices, and partly offsets the drag reduction due to displacement of the mean velocity profile induced by streamwise slip [37]. The effective slip length b^+ thus depends non-trivially on the local slip distribution as well as the viscous length scale of the inner flow, and an exact prediction usually warrants computational methods [37,38]. Moreover, the slip length at increasing flow speeds may also be influenced adversely by the curvature of the air–water interface spanning the groove troughs [39,40], occasional defects in the groove geometry, or the flow-induced collapse of the plastron in a small number of grooves [35]. Nevertheless, an estimate of the effective slip length—neglecting the complexities above—may be obtained [38] as $b \approx b_{\parallel} - b_{\perp} = (l/2\pi) \ln [\sec(\pi\phi/2)] = 22$ μm , which is quite consistent with the average slip length of $b = 17$ μm observed in our experiments.

3.4. Polymer + Superhydrophobic Rotor

Lastly, we performed drag measurements on the superhydrophobic grooved rotor in aqueous PAM solutions of various concentrations; a representative friction curve for $c = 50$ ppm is shown in Figure 2a. The individual friction curves for the no-slip rotor in 50 ppm PAM solution and for the superhydrophobic rotor in water—cases (B) and (C) above—are also included for comparison. As evident from the plot, the combined drag reduction resulting from the dissolved polymer and the plastron is larger than that attainable by either technique employed alone at all values of Re_τ (and in fact exceeds the MDR limit estimated for our TC geometry, as described in the Supplementary Materials), signifying that the two mechanisms can indeed operate additively to yield enhanced overall drag reduction in turbulent flows. From an engineering perspective, the quantity that is often of immediate interest is the net decrease in fluid friction—the wall shear stress in external flows, or the head loss per unit length in internal flows—compared to the flow of pure solvent (water) with no-slip flow boundaries under identical conditions of wall speed or flow rate. Accordingly, we define the percentage drag reduction $\mathcal{D} = (1 - \tau_w / \tau_{w,N}) \cdot 100\%$, where τ_w is the actual shear stress measured at the rotor wall, and $\tau_{w,N}$ is the reference wall shear stress on the no-slip rotor in deionized water at the same speed V (or equivalently, at the same solvent-based Reynolds number $Re_s = \rho V d / \eta_w$ computed using the viscosity η_w of water). In Figure 2b, the data from Figure 2a have been replotted as the percentage drag reduction \mathcal{D} versus the Reynolds number Re_s , and the enhancement in drag reduction from combining polymer additives and superhydrophobic surfaces is again apparent.

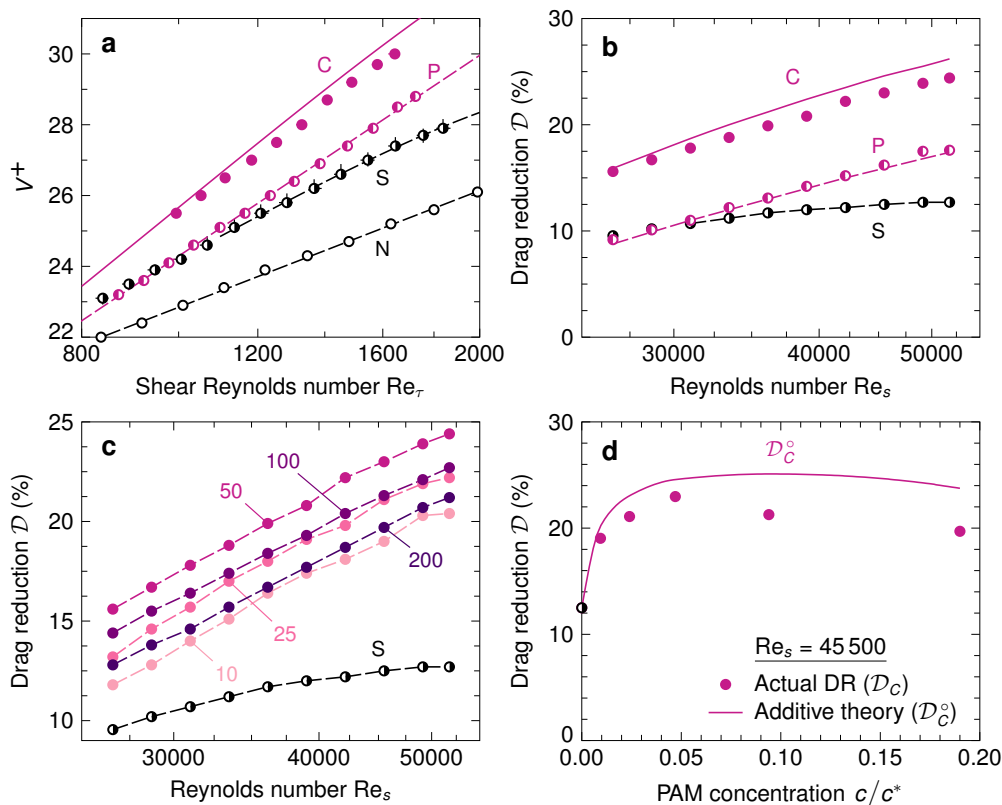


Figure 2. (a) Experimental friction curves and (b) the percentage drag reduction for the no-slip rotor in water (N) and in 50 ppm aqueous PAM (P), as well as for the superhydrophobic grooved rotor in water (S) and in 50 ppm aqueous PAM (C). The solid curves denote the ideal estimates $(V_C^+)^o$ and \mathcal{D}_C^o predicted by our additive model. (c) Combined percentage drag reduction for the superhydrophobic rotor in PAM solutions of various concentrations (labeled in ppm). (d) The actual percentage drag reduction \mathcal{D}_C , and the ideal estimate \mathcal{D}_C^o , as a function of c/c^* at $Re_s = 45,500$.

4. Discussion

We next proceed to formulate an empirical law to predict the combined drag reduction expected from a given polymer–wall pair, if their individual drag reduction efficacies are known beforehand. Insofar as both polymeric and superhydrophobic drag reduction results from complex modifications of the near-wall dynamics—induced respectively by dissolved macromolecules and interfacial slip—it is to be expected that their concurrent action will elicit mutual interactions that are amenable to quantitative prediction only through numerical methods [27]. Notwithstanding these complexities, we envision a simple two-layer model (see Figure 3) in which we assume that: (i) viscoelastic effects, which operate predominantly in the buffer layer and beyond [12,13], are largely oblivious to the influence of wall slip, which is confined mostly to the viscous sublayer [8–10]; and (ii) the average flux of streamwise momentum to the wall (i.e., the frictional shear stress) constitutes the principal mode of information exchange between the viscous sublayer and the outer flow. In this simple additive framework, we superimpose the velocity defects from Equations (2) and (3) to obtain the composite friction law:

$$(V_C^+)^{\circ} = V_P^+ + b^+ = V_P^+ + (V_S^+ - V_N^+), \tag{4}$$

representing the parallel action of the two drag-reducing mechanisms via a linear addition of the corresponding velocity increments expressed in wall units. Here, the subscript ‘C’ denotes ‘combined’ drag reduction, and the superscript $^{\circ}$ indicates an ideal estimate derived from the additive theory described above.

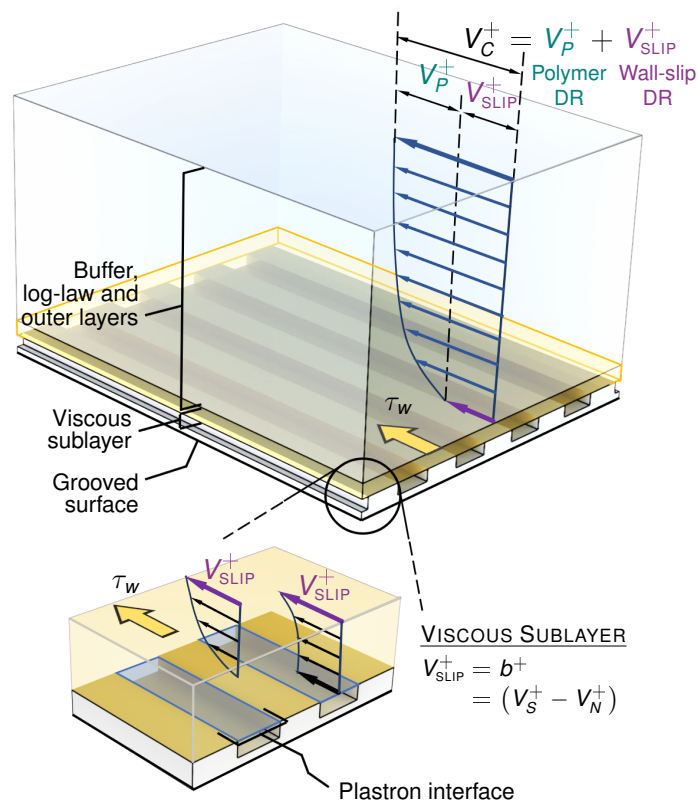


Figure 3. Schematic depiction of the additive two-layer model for combined drag reduction. The inset shows the thin near-wall viscous sublayer within which the composite boundary conditions are assumed to homogenize, yielding a uniform effective slip velocity V_{SLIP}^+ perceived by the outer layers. Dimensions are merely illustrative and are not to scale.

In Figure 2a,b, the solid curves represent the wall friction predicted by Equation (4), and the corresponding ideal estimate for the percentage drag reduction D_C° ; while there is fair agreement with experimental data especially at moderate Reynolds numbers ($Re_s \leq 30,000$), the actual drag

reduction levels are seen to be somewhat smaller than that obtained from our two-layer model. This, in turn, suggests that ‘non-linear’ interactions between the two drag reduction mechanisms serve to counteract rather than reinforce one another, and the additive expression in Equation (4) consequently represents an upper bound for the combined drag reduction levels that are actually realizable in practice. In Figure 2c, we show the variation of the combined drag reduction \mathcal{D}_C with the Reynolds number Re_s for different concentrations c of the dissolved polymer. Drag reduction initially increases with rising polymer concentration, plateaus, and subsequently falls off at concentrations exceeding 50 ppm; this latter decline arises from the increasing shear viscosity η_0 of the solution, which progressively offsets the drag reduction produced by polymeric suppression of turbulence. The effect of polymer concentration can also be seen in Figure 2d, in which the model predictions and measured drag reduction levels are shown as a function of c/c^* at a fixed value of the Reynolds number $Re_s = 45,500$. Evidently, the additive law provides a good estimate of the friction reduction attainable in dilute solutions, but slightly overpredicts the combined effect as the polymer concentration is raised.

In closing, we note that although periodically patterned textures—exemplified by the streamwise groove array employed in our study—serve as useful canonical surfaces with tunable slip properties, high fabrication cost and limited scalability render them impracticable in large-scale engineering applications. There is thus a practical imperative to explore combined drag reduction strategies that use scalable surfaces possessing irregular textural roughness. Furthermore, a number of common drag-reducing polymers, including PEO [41], are known to depress the surface tension of aqueous solutions, and their use may entail interfacial effects that adversely influence the overall slip at the wall [42]; our choice of PAM was prompted, in fact, by its notable lack of adsorption at the air–water interface [43]. Such practical considerations clearly merit further investigation, and we address some of these questions in a forthcoming article.

Supplementary Materials: Further details on experimental flow measurements using the TC apparatus, the viscometric characterization of PAM solutions, and the fabrication of the grooved superhydrophobic surface, as well as a discussion on polymer-mediated drag reduction in Taylor–Couette turbulence, are included in the Supplementary Material available online at <http://www.mdpi.com/2311-5521/5/4/197/s1>. Additionally, raw datasets from experimental friction measurements in the TC apparatus are provided separately as a Microsoft Excel spreadsheet.

Author Contributions: Conceptualization, A.R. and G.H.M.; methodology, A.R.; investigation, A.R.; supervision, G.H.M.; writing—original draft preparation, A.R.; writing—review and editing, G.H.M. All authors have read and agreed to the published version of the manuscript.

Funding: Financial support for this work was provided in part by the MRSEC program of the National Science Foundation (NSF) under award number DMR-1419807, and by the Office of Naval Research (ONR) under the MURI program through contract number 3002453814.

Acknowledgments: The authors would like to thank T. Van Buren and A. J. Smits at Princeton University for providing the grooved rotor used in this study.

Conflicts of Interest: The authors declare no conflict of interest. The funding sources had no role in the design of the study; in the collection, analyses, or interpretation of data; in the writing of the manuscript, or in the decision to publish the results.

References

1. Tennekes, H.; Lumley, J.L. *A First Course in Turbulence*; The MIT Press: Cambridge, MA, USA, 1972.
2. Pope, S.B. *Turbulent Flows*; Cambridge University Press: Cambridge, UK, 2000.
3. Stone, P.A.; Waleffe, F.; Graham, M.D. Toward a structural understanding of turbulent drag reduction: nonlinear coherent states in viscoelastic shear flows. *Phys. Rev. Lett.* **2002**, *89*, 208301. [[CrossRef](#)] [[PubMed](#)]
4. Roy, A.; Morozov, A.; van Saarloos, W.; Larson, R.G. Mechanism of polymer drag reduction using a low-dimensional model. *Phys. Rev. Lett.* **2006**, *97*, 234501. [[CrossRef](#)] [[PubMed](#)]
5. Kim, K.; Adrian, R.J.; Balachandar, S.; Sureshkumar, R. Dynamics of hairpin vortices and polymer-induced turbulent drag reduction. *Phys. Rev. Lett.* **2008**, *100*, 134504. [[CrossRef](#)] [[PubMed](#)]
6. Xi, L.; Graham, M.D. Active and hibernating turbulence in minimal channel flow of Newtonian and polymeric fluids. *Phys. Rev. Lett.* **2010**, *104*, 218301. [[CrossRef](#)] [[PubMed](#)]

7. Xi, L.; Graham, M.D. Dynamics on the laminar-turbulent boundary and the origin of the maximum drag reduction asymptote. *Phys. Rev. Lett.* **2012**, *108*, 028301. [[CrossRef](#)]
8. Martell, M.B.; Rothstein, J.P.; Perot, J.B. An analysis of superhydrophobic turbulent drag reduction mechanisms using direct numerical simulation. *Phys. Fluids* **2010**, *22*, 065102. [[CrossRef](#)]
9. Park, H.; Park, H.; Kim, J. A numerical study of the effects of superhydrophobic surface on skin-friction drag in turbulent channel flow. *Phys. Fluids* **2013**, *25*, 110815. [[CrossRef](#)]
10. Rastegari, A.; Akhavan, R. On the mechanism of turbulent drag reduction with super-hydrophobic surfaces. *J. Fluid Mech.* **2015**, *773*, R4. [[CrossRef](#)]
11. Perlin, M.; Dowling, D.R.; Ceccio, S.L. Freeman scholar review: Passive and active skin-friction drag reduction in turbulent boundary layers. *J. Fluids Eng.* **2016**, *138*, 091104. [[CrossRef](#)]
12. Graham, M.D. Drag reduction and the dynamics of turbulence in simple and complex fluids. *Phys. Fluids* **2014**, *26*, 101301. [[CrossRef](#)]
13. Xi, L. Turbulent drag reduction by polymer additives: Fundamentals and recent advances. *Phys. Fluids* **2019**, *31*, 121302.
14. Hoyt, J.W. The effect of additives on fluid friction. *J. Basic Eng.* **1972**, *94*, 258–285. [[CrossRef](#)]
15. Virk, P.S. Drag reduction fundamentals. *AIChE J.* **1975**, *21*, 625–656. [[CrossRef](#)]
16. White, C.M.; Mungal, M.G. Mechanics and prediction of turbulent drag reduction with polymer additives. *Annu. Rev. Fluid Mech.* **2008**, *40*, 235–256. [[CrossRef](#)]
17. Han, W.J.; Choi, H.J. Role of bio-based polymers on improving turbulent flow characteristics: Materials and applications. *Polymers* **2017**, *9*, 209. [[CrossRef](#)] [[PubMed](#)]
18. Han, W.J.; Dong, Y.Z.; Choi, H.J. Applications of water-soluble polymers in turbulent drag reduction. *Processes* **2017**, *5*, 24. [[CrossRef](#)]
19. McHale, G.; Newton, M.I.; Shirtcliffe, N.J. Immersed superhydrophobic surfaces: Gas exchange, slip and drag reduction properties. *Soft Matter* **2010**, *6*, 714–719. [[CrossRef](#)]
20. Rothstein, J.P. Slip on superhydrophobic surfaces. *Annu. Rev. Fluid Mech.* **2010**, *42*, 89–109. [[CrossRef](#)]
21. Bhushan, B.; Jung, Y.C. Natural and biomimetic artificial surfaces for superhydrophobicity, self-cleaning, low adhesion, and drag reduction. *Prog. Mater. Sci.* **2011**, *56*, 1–108. [[CrossRef](#)]
22. Golovin, K.B.; Gose, J.W.; Perlin, M.; Ceccio, S.L.; Tuteja, A. Bioinspired surfaces for turbulent drag reduction. *Phil. Trans. R. Soc. A* **2016**, *374*, 20160189. [[CrossRef](#)]
23. Watanabe, K.; Udagawa, H. Drag reduction of Non-Newtonian fluids in a circular pipe with a highly water-repellent wall. *AIChE J.* **2001**, *47*, 256–262. [[CrossRef](#)]
24. Seo, J.; García-Mayoral, R.; Mani, A. Pressure fluctuations and interfacial robustness in turbulent flows over superhydrophobic surfaces. *J. Fluid Mech.* **2015**, *783*, 448–473. [[CrossRef](#)]
25. Park, H.; Sun, G.; Kim, C.J. Superhydrophobic turbulent drag reduction as a function of surface grating parameters. *J. Fluid Mech.* **2014**, *747*, 722–734. [[CrossRef](#)]
26. Rajappan, A.; Golovin, K.; Tobelmann, B.; Pillutla, V.; Abhijeet.; Choi, W.; Tuteja, A.; McKinley, G.H. Influence of textural statistics on drag reduction by scalable, randomly rough superhydrophobic surfaces in turbulent flow. *Phys. Fluids* **2019**, *31*, 042107. [[CrossRef](#)]
27. Davis, E.A.; Park, J.S. Turbulence dynamics of dilute polymer solutions: Apparent slip and the effect of slip-inducing surfaces. In Proceedings of the 91st Annual Meeting of the Society of Rheology, Raleigh, NC, USA, 20–24 October 2019.
28. Srinivasan, S.; Kleingartner, J.A.; Gilbert, J.B.; Cohen, R.E.; Milne, A.J.B.; McKinley, G.H. Sustainable drag reduction in turbulent Taylor-Couette flows by depositing scalable superhydrophobic surfaces. *Phys. Rev. Lett.* **2015**, *114*, 014501. [[CrossRef](#)]
29. Rajappan, A.; McKinley, G.H. Epidermal biopolysaccharides from plant seeds enable biodegradable turbulent drag reduction. *Sci. Rep.* **2019**, *9*, 18263. [[CrossRef](#)]
30. Panton, R.L. Scaling laws for the angular momentum of a completely turbulent Couette flow. *C. R. Acad. Sci. Paris Ser. II* **1992**, *315*, 1467–1473.
31. Lathrop, D.P.; Fineberg, J.; Swinney, H.L. Transition to shear-driven turbulence in Couette-Taylor flow. *Phys. Rev. A* **1992**, *46*, 6390–6405. [[CrossRef](#)]
32. Lewis, G.S.; Swinney, H.L. Velocity structure functions, scaling and transitions in high Reynolds number Couette-Taylor flow. *Phys. Rev. E* **1999**, *59*, 5457–5467. [[CrossRef](#)]

33. McCarthy, K.J.; Burkhardt, C.W.; Parazak, D.P. Mark-Houwink-Sakurada constants and dilute solution behavior of heterodisperse poly(acrylamide-co-sodium acrylate) in 0.5 M and 1 M NaCl. *J. Appl. Polym. Sci.* **1987**, *33*, 1699–1714. [[CrossRef](#)]
34. Rubinstein, M.; Colby, R.H. *Polymer Physics*; Oxford University Press: Oxford, UK, 2003.
35. Buren, T.V.; Smits, A.J. Substantial drag reduction in turbulent flow using liquid-infused surfaces. *J. Fluid Mech.* **2017**, *827*, 448–456. [[CrossRef](#)]
36. Philip, J.R. Flows satisfying mixed no-slip and no-shear conditions. *Z. Angew. Math. Phys.* **1972**, *23*, 353–372. [[CrossRef](#)]
37. Min, T.; Kim, J. Effects of hydrophobic surface on skin-friction drag. *Phys. Fluids* **2004**, *16*, L55. [[CrossRef](#)]
38. Fairhall, C.T.; García-Mayoral, R. Spectral analysis of the slip-length model for turbulence over textured superhydrophobic surfaces. *Flow Turbul. Combust.* **2018**, *100*, 961–978. [[CrossRef](#)]
39. Sbragaglia, M.; Prosperetti, A. A note on the effective slip properties for microchannel flows with ultrahydrophobic surfaces. *Phys. Fluids* **2007**, *19*, 043603. [[CrossRef](#)]
40. Steinberger, A.; Cottin-Bizonne, C.; Kleimann, P.; Charlaix, E. High friction on a bubble mattress. *Nat. Mater.* **2007**, *6*, 665–668. [[CrossRef](#)] [[PubMed](#)]
41. Kim, M.W.; Cao, B.H. Additional reduction of surface tension of aqueous polyethylene oxide (PEO) solution at high polymer concentration. *Europhys. Lett.* **1993**, *24*, 229–234. [[CrossRef](#)]
42. Peaudecerf, F.J.; Landel, J.R.; Goldstein, R.E.; Luzzatto-Fegiz, P. Traces of surfactants can severely limit the drag reduction of superhydrophobic surfaces. *Proc. Natl. Acad. Sci. USA* **2017**, *114*, 7254–7259. [[CrossRef](#)]
43. Hu, R.Y.Z.; Wang, A.T.A.; Hartnett, J.P. Surface tension measurement of aqueous polymer solutions. *Exp. Therm. Fluid Sci.* **1991**, *4*, 723–729. [[CrossRef](#)]

Publisher’s Note: MDPI stays neutral with regard to jurisdictional claims in published maps and institutional affiliations.



© 2020 by the authors. Licensee MDPI, Basel, Switzerland. This article is an open access article distributed under the terms and conditions of the Creative Commons Attribution (CC BY) license (<http://creativecommons.org/licenses/by/4.0/>).